Applied Physics A (2021) 127:30
https://doi.org/10.1007/s00339-020-04137-6

Applied Physics A
Materials Science & Processing

LO-Phonons and dielectric polarization effects on the electronic properties of doped GaN/InN spherical core/shell quantum dots in a nonparabolic band model

A. Talbi[1,2] · M. El Haouari[1,3] · K. Nouneh[2] · L. M. Pérez[4] · A. Tiutiunnyk[4] · D. Laroze[4] · M. Courel[5] · M. E. Mora-Ramos[6,7] · E. Feddi[1]

Received: 4 September 2020 / Accepted: 7 November 2020 / Published online: 3 January 2021
© Springer-Verlag GmbH Germany, part of Springer Nature 2021

Abstract
The electron energy spectrum of a core/shell spherical quantum dot made of zincblende *GaN*/*InN* compounds is investigated taking into account the presence of an off-center donor atom and the influence of band nonparabolicity. The interaction of both the charge carrier and the Coulombic core with longitudinal optical phonons is included through Frö hlich and Aldrich-Bajaj theories, respectively. The ground state energy is determined by solving the resulting conduction band effective mass equation via the variational Ritz principle. A detailed analysis of the features of electron and hole spectra as functions of the core and shell sizes is presented, highlighting the possibility of transitioning between type-I and type-II structures. A detailed discussion about the effects of conduction band nonparabolicity, dielectric mismatch and electron-phonon interaction onto the impurity binding energy is provided. It was found that, in general, nonparabolicity of the conduction band leads to larger impurity binding energy, and that LO-phonon and dielectric mismatch effects tend to reduce the value of the latter quantity.

Keywords Spherical quantum dot · Core–Shell · Zincblende III–V nitrides · Polaron effects · Dielectric mismatch · Band nonparabolicity

✉ A. Tiutiunnyk
tyutyunnyk.a.m@academicos.uta.cl

✉ E. Feddi
e.feddi@um5s.net.ma

1 Group of Optoelectronic of Semiconductors and Nanomaterials, ENSAM de Rabat, Mohammed V University in Rabat, Rabat, Morocco

2 Laboratory of Materials Physics and Subatomics, Department of Physics, Faculty of Science, Ibn Tofail University, Kenitra, Morocco

3 Centre Régional des Métiers de l'Education et de Formation (CRMEF), Tanger, Morocco

4 Instituto de Alta Investigación, CEDENNA, Universidad de Tarapacá, Casilla 7 D, Arica, Chile

5 Centro Universitario de los Valles (CUValles), Universidad de Guadalajara, Carretera Guadalajara-Ameca Km. 45.5, C.P. 46600 Ameca, Jalisco, Mexico

6 Centro de Investigación en Ciencias-IICBA, Universidad Autónoma del Estado de Morelos, Av. Universidad 1001, Col. Chamilpa, CP 62209 Cuernavaca, Morelos, Mexico

7 Facultad de Ciencias Básicas, Universidad de Medellín, Medellín, Colombia

1 Introduction

Motivated by the development of efficient and environmentally friendly -large-scale- materials, advances achieved by scientists and industrials in the epitaxial growth technology and in chemical synthesis have allowed to imagine and realize new generations of quantum nanostructures, among which there are the so-called core/shell quantum dots (CSQDs). They are composed of two coated semiconductor materials with different band alignments. The manufacturing of these structures, base on the *band gap engineering* , permits to manipulate several combinations of II–VI, III–V or IV–VI semiconductors [1–5]. Given their inexpensive chemical techniques of obtaining, these new artificially made materials became very attractive for many futuristic applications [6–8]. In addition to the geometrical nature of a CSQD shape, the energy band gap can be adjusted by manipulating the core or/and the shell sizes. This operation provides the possibility to control the optoelectronic properties of these nanomaterials, related to the electron-hole recombination -which is affected by the alignment of the conduction and valence bands [9–11]. This *band gap engineering* technique

introduces many interesting physical consequences such as the control of the radiative recombination times. Currently, this kind of semiconducting systems appears forming part of various emergent photocatalytic and optoelectronic applications in different domains: solar cells [12, 13], optical encoding [14], Qbits [15], biosensors and tumor targeting [16, 17]. Being broadly investigated in the last decades, reviews on the production as well as physical properties of *CSQDs* have recently appeared [18, 19]. It has been demonstrated that CSQDs have a lot more advantages than single-material nanocrystal QDs. Indeed, these structures show a very high stability and stronger photoluminescence (*PL*), attributed to the better isolation from the surface effects of the charge carriers (electrons and holes), impurities, as well as excitons; confined inside the dot [20–22]. Other recent studies in QDs can be found in Refs. [23–26].

As in all heterostructures, the physical phenomena at the interfaces (core–shell and shell-external medium) influence the optoelectronic behavior of these nanosystems [27, 28]. In fact, for an encapsulated single dot, the shell size modifies considerably its energy spectrum. For instance, by increasing the *ZnS* dot size, Baranov *et al*. have shown a red shift on the *PL* spectra of *CdSe*/*ZnS* CSQDs [29]. In another interesting observation, Gaponik et al. detected a redshift of the *PL* peak in a *CdSe*/*ZnS*/*CdSe* structure, for large values of shell size [30]. On the other hand, it is of general knowledge that the optoelectronic properties of semiconductor-based systems are greatly influenced by the presence of impurity dopant atoms. This gives the chance to explore the tunability of electronic, optical and magnetic properties via selective doping, with its consequent effect on device applications. Beyond the doubts related to its actual realization, solitary dopant optoelectronics have become a reality, as reviewed by Koenraad and Flatté in their seminal paper [31]. So, it becomes also of interest to dedicate efforts to investigate impurity effects in low-dimensional semiconducting heterostructures and CSQDs in particular.

From a theoretical point of view, many works have been devoted to the problems of electron, hole, donor and exciton properties in *CSQDs* with different shapes (sphere, cylinder and ring). Cristea and Niculescu dealt with the donor impurity in *CdSe*/*ZnS* and *ZnS*/*CdSe* systems by taking into account the dielectric mismatch and the polarization effect [32–34]. The authors show that the peak of *PL* undergoes a redshift for low dielectric medium. The binding energy of donor states in a *ZnS*/*CdSe* CSQD increases even in the presence of an applied electric field. The increasing of the shell thickness of *ZnO*/*ZnS* core/shell dots leads to a reinforcing of the linear and nonlinear optical properties independently of the dielectric surrounded medium [35].

The role of the dielectric mismatch on the mobility of charge carriers and on the impurity binding energy in the coated semiconductor wires has been studied by Kirakosyan et al. [36, 37]. More recently, in a serie of papers, Feddi et al. have studied a number of problems related to the behavior of donor and exciton in these structures [38–44]. Among those problems one finds the case of the hydrogenic off-center donor placed anywhere in an inverted type-I ZnS/CdSe core/shell nanostructure, investigated with the use of the Ritz variational principle, taking into account the electron effective mass mismatch and the discontinuity of dielectric environment at the core/shell junction. We have also dealt with the magnetic effect on a single donor impurity placed anywhere in a spherical core/shell. In this study, we have shown that the optoelectronic properties of the CSQD depend on the simultaneous effects of shell thickness, magnetic field strength and dopant position. Concerning the excitonic effects, we have investigated the spatial separation effect on the energies of uncorrelated and correlated electron-hole pairs in CdSe/ZnS and InAs/InP type-I core/shell spherical quantum dots. Our analytical study allowed us to evaluate the critical values of the core size corresponding to the escape of the electron and hole from the core to the shell material [42].

When dealing with -weakly ionic- nitride-based *CSQD*, one should keep in mind the possibility that these structures will exhibit non-negligible polaronic corrections to effective mass and energy of slow charge carriers in the system, associated to the electron-phonon renormalization [45–47]. In our previous theoretical work, we have analyzed the bound polaron properties in zincblende GaN/InN CSQDs, including conduction band nonparabolicity effects [48]. As an initial approach, in our investigation we neglected the possible effects of the dielectric mismatch between the involved materials. However, according to the most recent accessible data, it is found that there is a substantial difference in the values of the dielectric constants of these cubic III–V nitrides, with respect to those of typical wide gap non-polar surrounding matrices used.

The phenomenon of dielectric mismatch between the semiconductor layers on both sides of a heterojunction's interface (either core/shell or shell/external medium one) implies the modification of the electron-impurity electrostatic interaction potential, due to the image charges induced at the boundary. In consequence, there will be self-polarization corrections to such potential energy term. The dielectric mismatch effects in semiconductor quantum dots have been investigated in the cases of cubic and spherical geometries [49–51]. Quantum dots of cylindrical shape were considered by Sil et al. [52]. For *CSQDs*, the influence of dielectric confinement on electron and impurity-related states was investigated by Cristea and collaborators [32, 34, 53, 54]. The simultaneous influence of dielectric mismatch and polaron effects on the impurity-related optical response of spherical *QDs* are reported in Ref. [55].

According to the comments made above, a more complete study of the electron-ionized donor in nitride-based *CSQDs* should include both polaron and dielectric confinement effects. Hence, in this work we are presenting a new investigation of the energy states corresponding to a conduction electron bound to a single donor center in spherical *GaN*/*InN CSQDs*, taking into account the conduction band nonparabolicity as well as electron-LO-phonon corrections. To describe the electrostatic phenomena involved at all interfaces, (core/shell and shell/surrounding nonpolar dielectric matrix), we will take into account the dielectric mismatch between all these different media. In accordance, the organization of the article is the following: Next section contains the theoretical approach used to determine bound polaron states. In Sect. 3 we present and discuss our results, whereas Sect. 4 is devoted to outline the conclusions of the work.

2 Theoretical framework

As mentioned, the present study concerns the polaronic effects on an off-center single dopant D^0 in core/shell *GaN*/*InN* quantum dots with inner radius a and outer radius b. The structure is assumed to be embedded within a dielectric material bearing a wide band gap. *GaN* (core) and *InN* (shell) are characterized by two different high-frequency dielectric constants, ε_c and ε_s respectively. In the Fig. 1, we are presenting a schematic representation of the system. To study the influence on the optoelectronic properties of the difference between dielectric constants of the external medium and the *CSQD* via the image-charge effects, we define an effective dielectric constant for all the (*GaN*/*InN*) structure as $\varepsilon_{in} = \sqrt{\varepsilon_c \varepsilon_s}$ [56, 57], whereas ε_{out} denotes the dielectric constant of the surrounding medium.

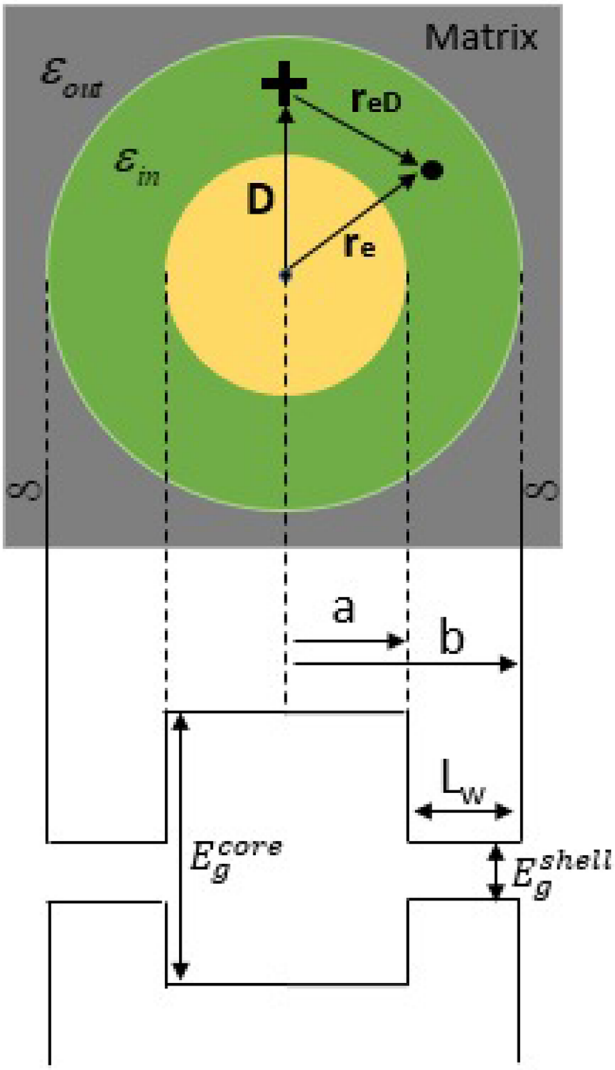


Fig. 1 Schematic representation of core/shell quantum dot structure with the corresponding band offsets

According to the effective-mass approximation and the Fröhlich's theory of electron-LO phonon coupling (polaron) [58], the Hamiltonian of the donor writes as:

$$H = H_0 + V_c + H_{ph} + H_{e-ph} \tag{1}$$

where the electronic Hamiltonian is given by

$$H_0 = -\frac{\hbar^2}{2m^i_{ep}(E)}\nabla^2 + V_w(r) + W(r) \tag{2}$$

Here, we shall adopt the model developed by the pioneer Bajaj and Aldrich works [59, 60]. Their model provides the necessary correction to the Coulombic coupling describing the electron-LO-phonon interaction. For the inclusion of phonon effects, we make use of a renormalized polaron effective mass $m(E)$. Moreover, we assume that the involved near-zone-center conduction band of the materials is affected by the phenomenon of nonparabolicity. To deal with such a feature, we shall rely on a description where the Γ-point effective mass is a function of the energy [61–63].

In our study, the energy-dependent polaron effective mass for *GaN* and *InN* is determined by considering the form [59]:

$$m^i_{ep}(E) = m^i_e(E)\frac{1 + \alpha_i/12}{1 - \alpha_i/12} \tag{3}$$

The parameter $\alpha_i = \frac{e^2\eta_i}{2\varepsilon_i^{'}\hbar\omega_{LO_i}}$ is the electron-LO-phonon dimensionless coupling coefficient (Fröhlich's constant). So, the energy-dependent effective mass for a given material A is given by [61–63]:

$$m_e^i(E) = m_e^{*i}\left(1 + \frac{E^i - V^i}{E_g^i}\right) \tag{4}$$

where E_g^i is the energy band gap of the considered material, m_e^* indicates the typical value of the material's conduction band effective mass, outcoming from the parabolic approximation, and V^i is the value of the confining potential energy function in the i-th region. In general, the mathematical expression of this parameter is given as a function of the radial position, as follows:

$$V_w(r) = \begin{cases} Q\Delta E_g & , \ 0 \le r \le a \\ 0 & , \ a < r \le b \\ \infty & , \quad r > b \end{cases} \tag{5}$$

Here, $Q = 0.7$ is the conduction band offset parameter. ΔE_g is the difference between the band gaps of GaN and InN, according to [64, 65]:

$$\Delta E_g(x) = E_g(GaN) - E_g(InN). \tag{6}$$

On the other hand, the term $W(r)$ denotes the self-energy of the electron resulting from kth interaction with its image-charge (see Appendix A) [41, 66–70];

$$W(r) = \frac{e^2(\varepsilon_{in} - \varepsilon_{out})}{2\varepsilon_{in} b} \sum_{k=0}^{\infty} \frac{k+1}{k\varepsilon_{in} + (1+k)\varepsilon_{out}} \left(\frac{r}{b}\right)^{2k} \tag{7}$$

In the Hamiltonian (1), the term V_c designates the contribution to donor energy resulting from the interactions between the charge carrier, together with the effect of the surrounding medium. It includes the Coulomb potential and the effect of polarization charges resulting from the dielectric mismatch between the *CSQD* constituents, as well as with the external dielectric medium (see Appendix A) [41, 66–70]:

$$V_c(r,\theta) = -\frac{e^2}{\varepsilon_{in} r_{eD}} - \frac{e^2(\varepsilon_{in} - \varepsilon_{out})}{\varepsilon_{in} b} \sum_{k=0}^{\infty} \frac{k+1}{k\varepsilon_{in} + (1+k)\varepsilon_{out}} \left(\frac{D.r_e}{b^2}\right)^k P_k(\cos(\theta)), \tag{8}$$

where $r_{eD} = \sqrt{r^2 + D^2 - 2rD\cos(\theta)}$ is the electron-donor distance, θ is the angle between the electron and impurity vector positions, $\mathbf{r}$ and $\mathbf{D}$ respectively. In addition, $P_k(cos(\theta))$ denotes the Legendre polynomial of k th-order.

The Hamiltonian of the non-interacting LO-phonon system is [71]:

$$H_{ph} = \sum_{i=c,s} \sum_{\mathbf{q}} \hbar\omega_{LO_i} \left(a_i^{\dagger}(\mathbf{q})\, a_i(\mathbf{q}) + \frac{1}{2}\right) \tag{9}$$

where $a_i^{\dagger}(\mathbf{q})$ and $a_i(\mathbf{q})$ are, respectively, the creation and annihilation operators -in each CSQD region- of a LO-phonon of wave vector $\mathbf{q}$ and frequency ω_{LO_i}. Finally the last term in Eq. (1) is the bulk-like Fröhlich interaction Hamiltonian describing the electron-LO-phonon coupling. It is given by [58]:

$$H_{e-ph} = \sum_{i=c,s} \sum_{\mathbf{q}} \left[V_{q,i} e^{i\mathbf{q}\cdot\mathbf{r}} a_i(\mathbf{q}) + V_{q,i}^* e^{-i\mathbf{q}\cdot\mathbf{r}} a_i^{\dagger}(\mathbf{q})\right]. \tag{10}$$

The interaction amplitude $V_{q,i}$ writes as follows:

$$V_{q,i} = -\frac{i\hbar\omega_{LO_i}}{q} \left(\frac{4\pi\alpha_i}{\Omega}\right)^{1/2} \left(\frac{\hbar}{2m_{ep}^i(x,E)\omega_{LO_i}}\right)^{1/4} \tag{11}$$

where Ω is the volume of the quantum dot. By using the Lee-Low-Pines canonical transformation [72], Aldrich and Bajaj derived an effective renormalized Coulombic potential energy operator (V_{eff}^i) containing both phonon and phonon-electron energies as well as the dielectric mismatch effects. Its expression for an off-center impurity in the ith-region of the QD is given by the expression (see Appendix B) [59, 73–75]:

$$V_{eff}^i = -\frac{e^2}{\varepsilon_{in} r_{eD}} - \frac{e^2(\varepsilon_{in} - \varepsilon_{out})}{\varepsilon_{in} b} \sum_{k=0}^{\infty} \frac{k+1}{k\varepsilon_{in} + (1+k)\varepsilon_{out}} \left(\frac{Dr_e}{b^2}\right)^k P_k(\cos(\theta)) - \frac{e^2}{\varepsilon_i' r_{eD}} \exp(-\eta_i r_{eD}) + \frac{e^2\eta_i}{2\varepsilon_i'} \frac{\exp(-\eta_i r_{eD})}{1 + \alpha_i/12 + \alpha_i/(4+\alpha_i/3)} - \alpha_i\hbar\omega_{LO_i} \tag{12}$$

and

$$\eta_i = \left(\frac{2m_{ei}^*\omega_{LO_i}}{\hbar}\right)^{1/2}. \tag{13}$$

Notice that we have introduced a relative dielectric constant, connected to the static and high frequency dielectric constants by the relation

$$\frac{1}{\varepsilon_i'} = \frac{1}{\varepsilon_{\infty,i}} - \frac{1}{\varepsilon_{0,i}} \tag{14}$$

To simplify the mathematical writing, we use the effective Bohr radius $a_D = \hbar^2\varepsilon_{in}/e^2 m_{ep_c}^c(E)$ as unit of length, and the effective Rydberg $R_D = e^2/2\varepsilon_{in} a_D^2$, as unit of energy. In these units, the Hamiltonian can be simplified as:

$$H_{eff}^i = H^i + V_{eff}^i, \quad i = c \text{ and } s$$

Thus, inside the core region, the electronic parts (impurity-related and the interaction of the electron itself with image charges) of the Hamiltonian take the following form:

$$H_c = -\Delta - \frac{2}{r_{eD}} - \frac{2(\varepsilon_{in}-\varepsilon_{out})}{b}\sum_{k=0}^{\infty}\frac{k+1}{k\varepsilon_{in}+(1+k)\varepsilon_{out}} \left(\frac{Dr_{eD}}{b^2}\right)^k P_k(\cos(\theta)) + \frac{2(\varepsilon_{in}-\varepsilon_{out})}{b}\sum_{k=0}^{\infty}\frac{k+1}{k\varepsilon_{in}+(1+k)\varepsilon_{out}}\left(\frac{r}{b}\right)^{2k} + V_w + V_{eff}^c \tag{15}$$

while the operator summarizing the self-energy of phonons and their interactions with donor can be written as:

$$V_{eff}^c = -\frac{\varepsilon_{in}}{\varepsilon_c' r_{eD}}\exp(-\eta_c r_{eD}) + \frac{\varepsilon_{in}}{\varepsilon_c'}\eta_c\frac{\exp(-\eta_c r_{eD})}{1+\alpha_c/12+\alpha_c/(4+\alpha_c/3)} - \alpha_c\hbar\omega_{LO_c}/R_D \tag{16}$$

On the other hand, inside the shell region these two contributions have the following forms:

$$H_s = -\sigma(E)\Delta - \frac{2}{r_{eD}} - \frac{2(\varepsilon_{in}-\varepsilon_{out})}{b}\sum_{k=0}^{\infty}\frac{k+1}{k\varepsilon_{in}+(1+k)\varepsilon_{out}} \left(\frac{Dr_{eD}}{b^2}\right)^k P_k(\cos(\theta)) + \frac{2(\varepsilon_{in}-\varepsilon_{out})}{b}\sum_{k=0}^{\infty}\frac{k+1}{k\varepsilon_{in}+(1+k)\varepsilon_{out}}\left(\frac{r}{b}\right)^{2k} + V_w + V_{eff}^s \tag{17}$$

and

$$V_{eff}^s = -\frac{\varepsilon_{in}}{\varepsilon_s' r_{eD}}\exp(-\eta_s r_{eD}) + \frac{\varepsilon_{in}}{\varepsilon_s'}\eta_s\frac{\exp(-\eta_s r_{eD})}{1+\alpha_s/12+\alpha_s/(4+\alpha_s/3)} - \alpha_s\hbar\omega_{LO_s}/R_D, \tag{18}$$

where $\sigma(E) = m_{ep_c}^c/m_{ep}^s$.

The ground state energy of a donor in interaction with LO phonons and its corresponding envelope wave function are solutions of the Schrödinger equation:

$$H_{eff}\Psi(r,\theta,\phi) = E_{D^0}\Psi(r,\theta,\phi). \tag{19}$$

This eigenvalue equation must be solved in the two regions of the structure. Analyzing the form of the Hamiltonian, we can easily notice that the resulting partial differential equation does not admit any analytical solution. Therefore, our approach will be based on the using of a variational method where the donor energy E_{D^0} results from minimizing the expectation value of H_{eff}. That is:

$$E_{D^0} = \min\frac{\langle\Psi|H_{eff}|\Psi\rangle}{\langle\Psi|\Psi\rangle}. \tag{20}$$

We recall that the performance of the variational procedure is related to the suitable choice of the trial wave function. The donor system is, in general, stable. So, restricting to work with the ground state of the system, only one term is sufficient. Under these conditions, we choose a variational wave function as a product of an -uncoupled- electronic part $\Psi_e(r,\theta,\phi)$ (which corresponds the wave function of an electron in core/shell structure) multiplied by a hydrogenic-like term describing the Coulombic interaction between the electron and ionized donor: $\exp(-\beta\sqrt{r^2+D^2-2rD\cos(\theta)})$. Consequently:

$$\Psi_{D^0}(r,\theta,\phi) = N\Psi_e(r,\theta,\phi)\exp(-\beta\sqrt{r^2+D^2-2rD\cos(\theta)}), \tag{21}$$

where N is a normalization constant.

To determine the uncoupled electron wave function, we recall briefly that it can be written in the well-known form: $\Psi(r,\theta,\phi) = R_n(r)Y_{l,m}(\theta_e,\phi_e)$. $R_n(r)$ is the radial part and $Y_{l,m}(\theta_e,\phi_e)$ are the spherical harmonics. Besides, n is the main quantum number and l, m are, respectively the azimuthal and magnetic quantum numbers. According to our above mentioned restriction, our state is characterized by: $n = 1, l = 0$ and $m = 0$. Also, we must keep in mind that, for the fundamental state $Y_{0,0}(\theta_e,\phi_e) = 1/\sqrt{4\pi}$.

The problem of an electron in a core/shell structure is complicated to treat. In fact the energy depends on the localization of the electron, depending on whether it is in the core or in the shell. The existence of the electron in the core or shell regions depends on its energy (E_e^{1s}) and on the core/shell sizes. Indeed two possible cases can be considered: the first one corresponds to $E_e^{1s} < V_{0e}$, the core radius a is lower than a critical value b (obtained from $E_e^{1s} = V_{0e}$) and, consequently, the electron locates within the shell region. So, we have:

$$\Psi_e(r) = \frac{1}{r}\begin{cases} N_1\sinh\left(k_1 r\right), & 0 \le r \le a \\ N_2\sin\left[k_2(b-r)\right], & a < r \le b, \end{cases} \tag{22}$$

where $k_1 = \sqrt{(V_{0e}-E_e^{1s})/R_D}$ and $k_2 = \sqrt{(E_e^{1s}/\sigma(E)R_D)}$. The second case corresponds to $E_e^{1s} > V_0$, when the core radius a is bigger than the critical value b. Then, the wave function reads:

$$\Psi_e(r) = \frac{1}{r}\begin{cases} N_3\sin\left(k_3 r\right), & 0 \le r \le a \\ N_4\sin\left[k_4(b-r)\right], & a < r \le b. \end{cases} \tag{23}$$

Here, $k_3 = \sqrt{(E_e^{1s} - V_{0e})/R_D}$ and $k_4 = \sqrt{(E_e^{1s}/\sigma(E)R_D)}$. In both cases N_i are normalization constants which can be determined via the condition $\langle\psi_e|\psi_e\rangle = 1$. The ground state energy, E_e^{1s}, comes from solving the transcendental equation obtained by imposing the continuity conditions on the wave function and the probability current density at the core surface:

$$[\Psi_{core}(r)]_{r=a^-} = [\Psi_{shell}(r)]_{r=a^+} \tag{24}$$

and

$$\left[\frac{1}{m^*_{ep_c}(E)}\frac{d\Psi_{core}(r)}{dr}\right]_{r=a^-} = \left[\frac{1}{m^*_{ep_s}(E)}\frac{d\Psi_{shell}(r)}{dr}\right]_{r=a^+}. \tag{25}$$

In the next section, we will discuss the numerical results.

3 Results and discussions

First of all, it is worth mentioning that the optoelectronic properties of this spherical nanostructures depend on the electron-hole radiative transitions, which are related to the nature of the material where the charge carriers are localized. Thus, let us discuss one fundamental point, often neglected in several theoretical studies. In fact, due to the physical parameters of the materials (band gap, effective masses and dielectric constants), electron and hole behave differently in their proper bands; according to variations of the core and shell sizes. In fact, adjusting the core or/and shell sizes via the ratio *a*/*b* leads to different spontaneous localization of electron and hole within the core or shell materials, thus leading to a possible transition of the *CSQD* from a type-*I* to a type-*II* heterostructure or vice versa (see Fig. 2 for illustration). The main input parameters used in our numerical evaluation appear in Table 1. Indeed, for a *CSQD* structure with finite band offsets and fixed external dimension *b*, electron and hole are localized in the shell region which constitutes the potential energy well, with thickness $(L_w = b - a)$, as indicated in Fig. 1. With increasing the core radius, hole (electron) energy levels decrease (increase). Then, when $E_e > V_{oe}$ ($E_h > V_{0h}$), electron (hole) leaves the shell material towards the core region, at two different critical core sizes a^e_{crit} and a^h_{crit} respectively. This difference between the critical radii is due to the different values of the band offset in the conduction and valence bands, and also to the difference between the electron and hole effective masses. These critical radii can be determined by imposing Ben Daniel-Duke boundary conditions and by considering that the energies of the two particles -taken separately- are equal to the band offsets, $E_e = V_0$ and $E_h = V_0$ [39, 42].

To clarify this mechanism in an inversed type-I core/shell of the (*GaN*/*InN*) type, we consider a structure with a very reduced core size ($a \longrightarrow 0$), as presented in Fig. 2. Because of the shape of the band alignment between the two materials, electron and hole are confined in the shell region. Then,

Table 1 Input parameters for zinc-blende GaN and InN (see Refs. [76–79])

	m^*_e/m_0	m^*_{lh}/m_0	ε_0	ε_∞	$Eg(eV)$	$\omega_{LO}(cm^{-1})$
GaN	0.193	0.265	9.44	5.31	3.3	742
InN	0.054	0.080	11.22	7.0	0.60	590

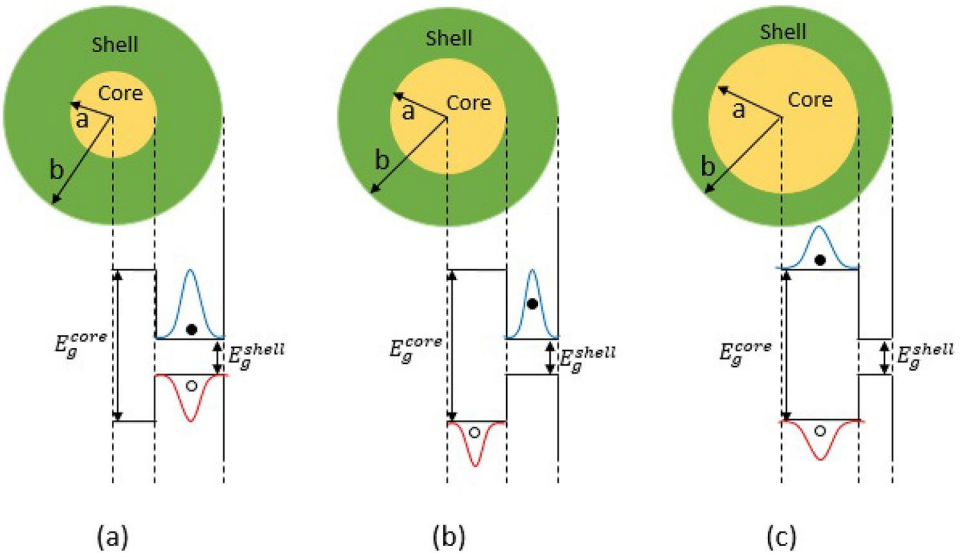


Fig. 2 Pictorial view of inversed type-I core/shell nanostructure for different particle localization possibilities, depending on the core radius: **a** corresponds to $a < a^e_{crit}$ and $a < a^h_{crit}$, meaning that electron and hole are both within the shell region. **b** Corresponds to $a < a^e_{crit}$ and $a > a^h_{crit}$, which means that hole escapes to the core while the electron remains within the shell (this situation is analogous to a type II core/shell structure). **c** Corresponds to $a > a^e_{crit}$ and $a > a^h_{crit}$, representing the case when electron and hole are both in the core region

we proceed by reducing the shell thickness. Thus, we fix b and increase the core size a; the hole (electron) energy level decreases (increases) until a given value $a = a^h_{crit}$ is reached, for which the hole escapes into the core while the electron remains confined in the well. This interesting situation corresponds to a type-II core/shell structure (see Fig. 2b). By increasing the core volume, the electron is allowed to pass towards the core region when the latter reaches the critical value a^e_{crit}. We note that our calculations (summarized in Table 2) show that the hole leaves to the shell before the electron does, whatever the size of the *CSQD*.

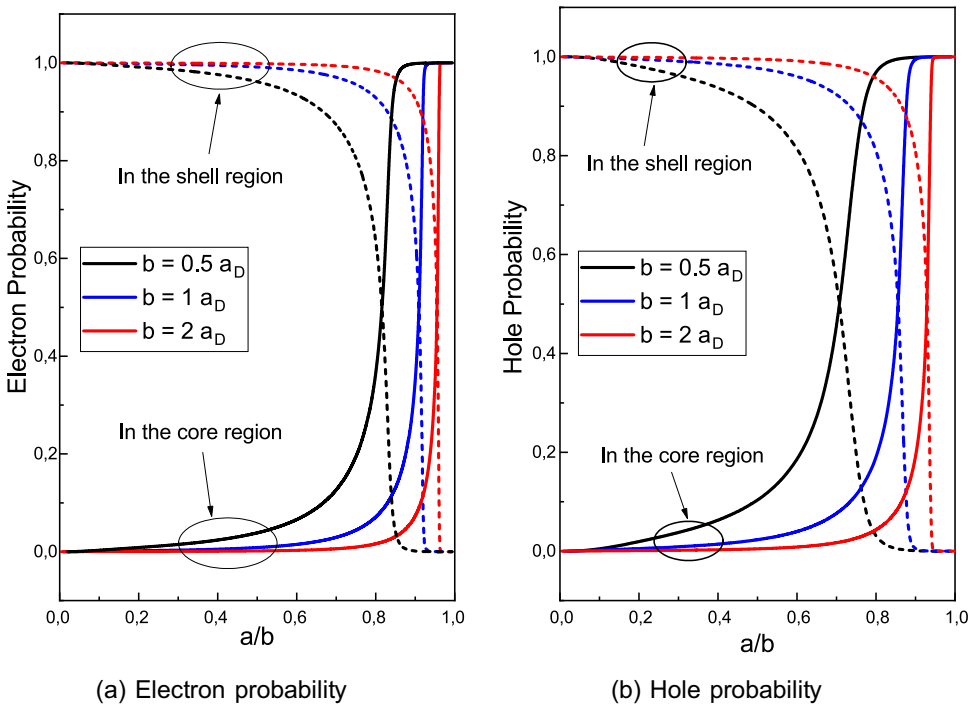
In connection with the above discussion, we present in Fig. 3a plot of the location probability as a function of the ratio a/b for the electron (Fig. 3a) and the hole (Fig. 3b) in the core and shell regions. A simple reading of these curves shows that these representations consolidate and allow us to understand the interpretation discussed previously. In the case of the electron, Fig. 3a shows that, for all different confinement regimes, the probability of the existence of the electron in the core region increases with increment of the ratio a/b, reaching its maximum at $a = a^e_{crit}$; which actually depends on the core size. It means that the electron escapes by tunnel effect towards the core region, so its probability density is larger within this part of the structure. Notice that, in the case of the strong confinement regime ($b = 0.5a_D$), the location of the electron in core or/and shell regions becomes equiprobable for a/b close to $0.78a_D$, while for $b = 2a_D$ the equiprobability takes place for a ratio close to 0.9. In Fig. 2b, we have plotted the hole probability in both shell and core regions. The same conclusion as in the electron case is still valid for holes. An important remark can be deduced by comparing Figs. a, b: for all values of *CSQD* sizes the a^h_{crit} is always lower than a^e_{crit}. This result is in good agreement with results shown in Table 2.

In Fig. 4, the variation of electron and hole energies is represented as a function of the ratio a/b for different values of the shell radius; $b = 0.5a_D$, $b = 1a_D$ and $b = 2a_D$, using a nonparabolic band model. Our numerical approach provides the possibility to control the variation of the optical band gap E_g of the *CSQD* structure as a function of the core to shell ratio a/b. It is noted that the energy of the electron in the conduction band increases and tends towards a constant value as long as the radius of the core exceeds the critical size, which depends on the shell width; as already discussed in previous curves. For the valence band, the energy decreases with the increase in the radius of the core a and stabilizes as soon as $a > a_{crit}$.

As one may observe, for the three values of shell sizes ($b = 0.5$, 1 and $2a_D$), the gap energy of the structure depends on the core size. E_g values vary from $0.61eV$ to $3.34eV$, when the ratio a/b increases from 0 to 1. The band diagram represented in Fig. 4 specifies the radiative transitions likely to be observed in the three optical domains. This fact is highly sought after in optoelectronic applications based on

Table 2 Critical values (in units of a_D) of core size at which electron and hole move inside the core region, for different shell widths

	$b = 0.5$	$b = 1$	$b = 2$
a^e_{crit}	0.391	0.887	1.891
a^h_{crit}	0.362	0.862	0.871



(a) Electron probability (b) Hole probability

Fig. 3 Electron and hole probability versus the ration a/b for different structure sizes $b = 0.5$, 1,and$2a_D$

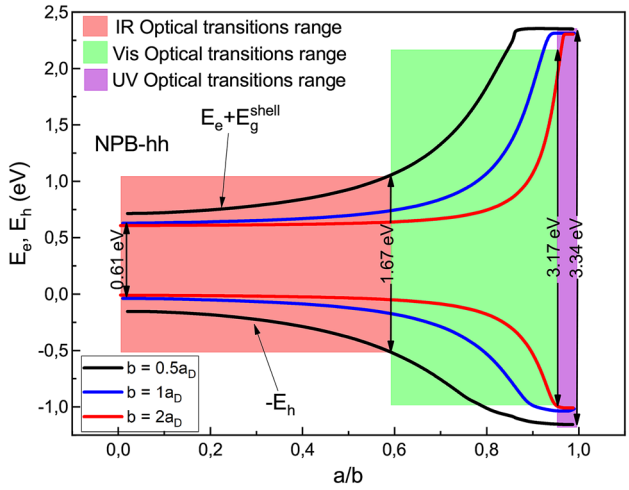


Fig. 4 Variation of optical gap energy as a function of the ratio a/b for different shell size $b = 0.5$, 1,and$2a_D$, considering conduction band nonparabolicity

semiconductor QDs. The band to band transition can be controlled by adjusting the core or shell widths. Within this set of sizes, we can have either an *IR* band, corresponding to the quantum dots having the gaps located between 0.61 and 1.61 eV, or a visible one, with a gap belonging to the interval [1.61 eV, 3.16 eV]. Besides a *UV* radiation would be obtained for very small shell thickness giving gaps located between 3.16 eV and 3.34 eV.

Let us consider now a *CSQD* doped with a single off-center donor D_0. Many configurations can be considered according to the position of the ionized impurity in the shell, $a < D < b$. All panels in Fig. 5 show that the distribution of the electronic density is very sensitive to the position of the ionized donor in both parabolic (PB) and nonparabolic band (NPB) cases. For this figure, we have chosen the values $a = 1a_d$ and $b = 2a_D$. The first column shows the electronic charge distribution in the *PB* case. As it can be seen, when the ionized donor is placed at the center of the shell ($D = (a + b)/2$), the electronic density is more localized around the impurity with spherical distribution and the orbitals become shrunk. However, when the donor moves to one of extremities (a or b), the orbital overlap spatially expands. The densities are more extended in these cases and lose their spherical symmetries. We also notice that the probability density is slightly more extended when the ionized donor is placed at the extremity of the shell ($D = a$) than in the situation when it is localized at the extremity of the core ($D = a$). To analyze the effect of the NPB on the densities, we present in column 2 of Fig. 5 the panels of the density of probability for the three positions $D = (a + b)/2$, $D = a$ and $D = b$. The comparison between columns 1 and 2 shows clearly that the NPB character shrinks and retracts electronic orbitals of the donor, thus implying a narrower spatial localization. To complete our description we have plotted in Fig. 6 the radial density of probability with and without taking into account the NPB effects. The curves show that this quantity decreases in magnitude in the case of the NPB model. This means that the retraction of the electron cloud caused by the NPB character is a result of the change in band symmetry, which leads to a reduction of the electron energy. Another effect was detected by analyzing Fig. 6a, b. The maxima of probabilities depend strongly on the impurity position in the shell. In the PB case, the probabilities admit a rather symmetrical aspect for all positions of the donor, with a maximum of the probability for $D = (a + b)/2$. In the case of NPB, the symmetry of the radial probability density is obtained only for $D = (b + a)/2$. In the case when the impurity is localized at the extremities of the well the radial probability loses its symmetry and its maximum tends to approach the shell outer radius when $D = b$ and to the extremity of the core when $D = a$.

In Fig. 7, we have presented the variation of the electron-impurity binding energy as a function of the donor position for a given size setup of the CSQD ($a = 1a_D$ and $b = 2a_D$). The position of the ionized donor sweeps the shell region range from a to b. Important features and conclusions can be extracted from these curves. First, we remark that with PB and NPB effects, the curves representing the binding energies admit almost symmetrical shapes around $D = (a + b)/2$ which is, approximately, the abscissa of all maxima. This conclusion is in good agreement with the behavior of the electron probability density described previously. In addition, when the ionized donor is placed at the extremities, $D = a$ or $D = b$; the effective distance separating the electron and the donor center enhances which leads to spatial spreading of the electron density and to a weakening of the electrostatic interaction with the Coulomb core. Consequently, the coupling becomes less significant and binding energy diminishes. The second remark that can be extracted is that our results clearly show that the effect of the NPB reduces the binding energy whatever is the position of the donor in the structure. This reduction is more pronounced when the ionized donor is localized at the center of well at $(a + b)/2$, compared to the other donor positions. This indicates that NPB changes the effective electron-impurity distance in a way that it augments, compared to the PB-based description. That is, as noticed from Fig. 6 the spatial distribution of the electron probability density around the core enter is smaller. The third interesting finding demonstrates the importance of the interaction with phonons and the influence of the DMM on the energy spectrum. As can be seen in Fig. , these effects reduce drastically the binding energy in both PB and NPB descriptions. This influence is more pronounced when the impurity is localized at the center of the shell ($D = (b + a)/2$). We also emphasize that the binding energy is more sensitive to the phonon and DMM effects in

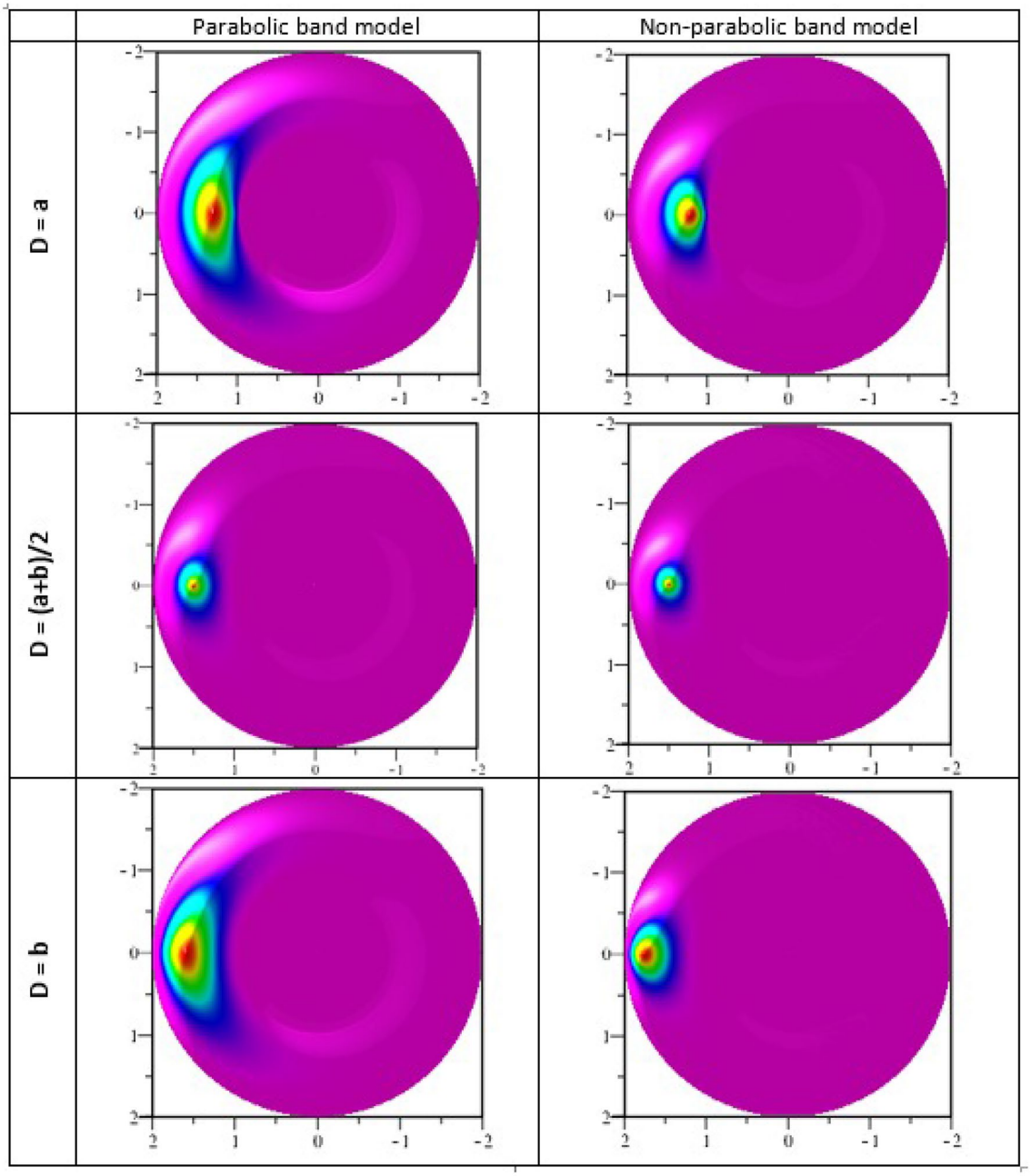


Fig. 5 Cross section of probability density for different values of ionized donor position with and without the use of the nonparabolic conduction band model

the case of NPB. What is actually happening, in this case, is that the renormalization of the potential energy due to dielectric mismatch and electron-phonon interaction implies a weakening of the Coulombic bound between the electron and the ionized donor.

Actually, several simultaneous effects coexist and contribute to the behavior of the binding energy: the external radius of the structure (b), which conditions the 3D confinement; the ratio a/b, which defines the shell thickness; the nature of the curvature of the band (PB or NPB); the interaction with LO phonons; and the influence of the DMM. To investigate the nature of the contributions of LO phonons and DMM to the system's energy, it seems very useful to us to clarify the separate behavior of these two factors. The Fig. 8 represents the -variationally- calculated optical phonon energy as a function of a/b, under two distinct confinement regime limits: strong confinement ($b = 1a_D$) and moderate confinement ($b = 2a_D$), fixing the donor position

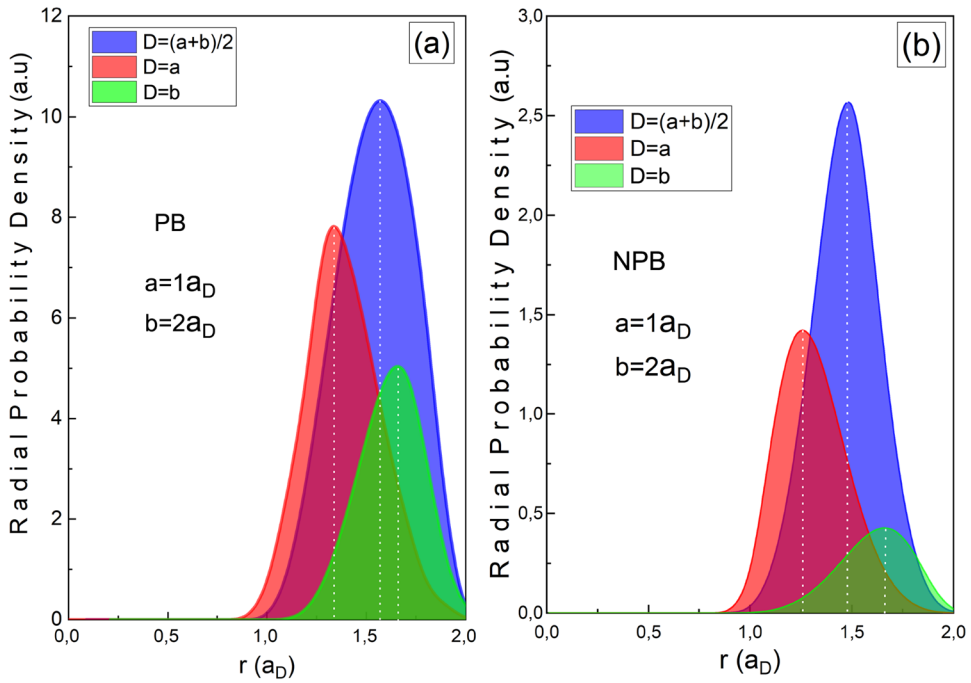


Fig. 6 The radial probability density for different donor positions: **a** parabolic band case and **b** nonparabolic band case

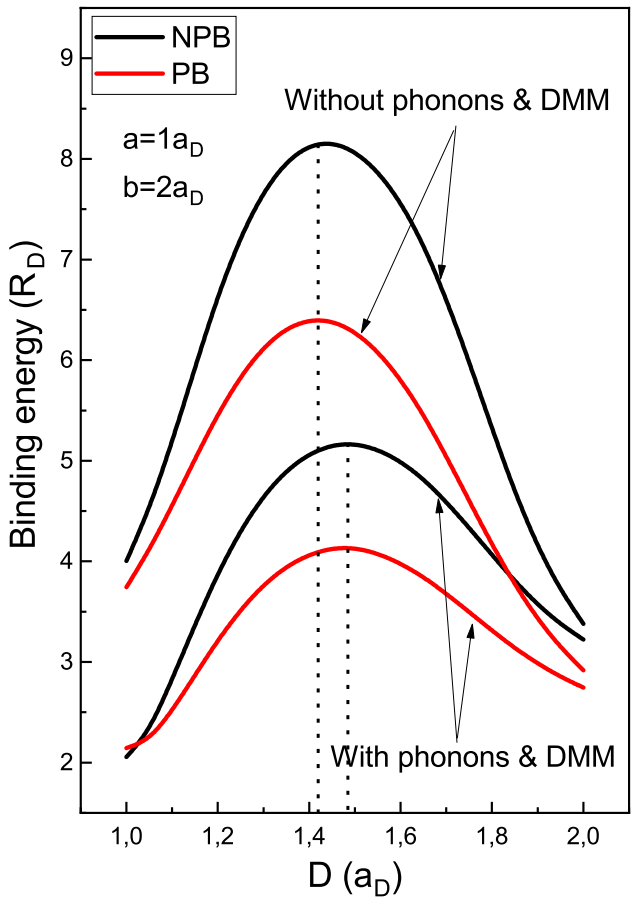


Fig. 7 Variation of impurity binding energy versus donor position for $a = 1a_D$ and $b = 2a_D$: The calculation included electron-phonon, dielectric mismatch (DMM) and conduction band parabolicity/nonparabolicity (PB/NPB) effects

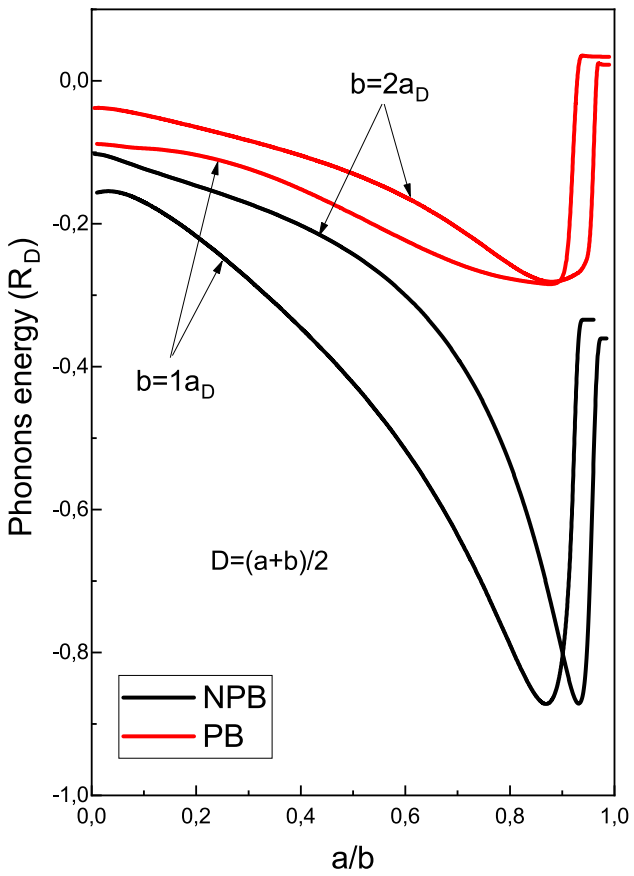


Fig. 8 Contribution of electron-LO-phonons energy as a function of a/b ratio for $b = 1a_D$, and $2a_D$ with and without conduction band nonparabolicity effect

at $D = (a + b)/2$. As noticed, this effect has a negative contribution for every value of the ratio and for all types of confinements. It exhibits a decreasing behavior which reaches a minimum at the critical value a_{crit}. Between a_{crit}/b and 1, the interaction with phonons increases drastically with a saturation tendency when a/b tends to 1, which is equivalent to a situation in which we have an isolated *GaN* QD, for which the electron-phonon interaction gives a fixed energy correction with repulsive character in the case of the parabolic description of band profile. This value implies a slight modification related to the weak coupling between the on-border donor and bulk LO-phonons. Interestingly, the use of a nonparabolic conduction band model keeps the electron-phonon correction within negative values all the way along with the interval of a/b values; but the saturation tendency at $a/b = 1$ remains. It is worth highlighting that the NPB effect leads to larger negative values of this contribution in all regimes of confinement, compared with PB results. Accordingly, our numerical investigation shows an important conclusion related the NPB: taking into account the NPB induces a strong correlation between the donor and LO-phonons. The behavior conserves its tendency with an important decreasing compared to the PB case and reaches its minima at the $(a/b)_{crit}$ and an increasing drastically with an obvious saturation close to $a/b = 1$. This phenomenon is explained by the fact that the phonon contributions depend on the structure size as mentioned by several authors [71].

Another feature deserves to be commented in detail. For instance, the larger magnitude of the electron-phonon-related energy in the case of strong confinement, which relates with the increment in electron localization [see, as a reference, the Eqs. (18, 20)]. The reverse in the monotony of phonon-related energy that takes place for the larger values of a/b ratio above a_{crit}/b has to do, precisely, with the reduction in electron probability around the ionized donor, as depicted in Fig. 3a. For the sake of approaching the real situation, we have introduced in our approach the *DMM*. This contribution is summarized in Fig. 9. The variation of DMM-related energy is also given for two distinct confinement regimes: $b = 1a_D$ and $b = 2a_D$ and, in both cases, with and without the parabolic band hypothesis. From this figure, we can note that the effects of the polarization charges have an attractive character. The related correction has negative values in regardless of the confinement strength and the dot size. It is more important in the strong confinement case. In addition, this contribution depends on the *QD* size and on the ratio a/b. The general aspect of the evolution of the *DMM* terms looks pretty alike as the LO-phonons contribution, but without any crossing at $(a/b)_{crit}$; but its numerical weight is significantly higher than the phonon-related one. The influence of *NPB* effect is, also, to enhance the magnitude of the *DMM* contribution. However, in proportion to the dielectric-matched case, this influence is weaker compared to that coming from

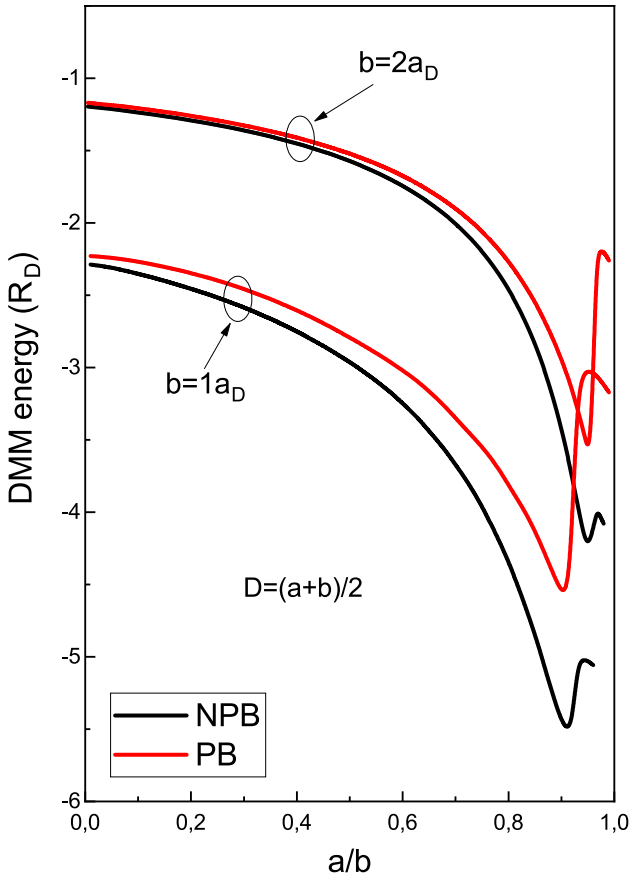


Fig. 9 The same as in Fig. 8 protect but for the contribution of dielectric mismatch effect

LO-phonon effects in its case. The Figs. 10, 11, 12 and 13 contain the results for the impurity-related electron binding energy in the *GaN/InN CSQD*, calculated under distinct environments. In all cases, E_b appears as a function of the ratio, a/b, between core and shell radii, whilst the impurity position is chosen to be $D = (a + b)/2$ and we fix $b = 2_D$. In Figs. 10 and , we present, separately, the results obtained with and without the inclusion of band nonparabolicity. As it was extensively discussed in our previous work the inclusion of polaronic corrections causes a noticeable decrease of E_b [48]. At this point, we believe that clarification is necessary. The magnitude of the polaronic correction, as noticed from Fig. 10, is always above $3R_D$, whereas the calculation of the separate phonon energy is significantly smaller as seen in Fig. 8. The reason for such a difference is that Fig. presents the variation of the (polaronic term) alone, as a function of a/b, with and without a parabolic band model. It is true that the phonon energy alone seems to be small compared to its effect but we should keep in mind that, when we introduce the LO-phonons effect, the whole system changes and all terms are affected because we are actually minimizing the total energy -which contains all energies terms- with respect

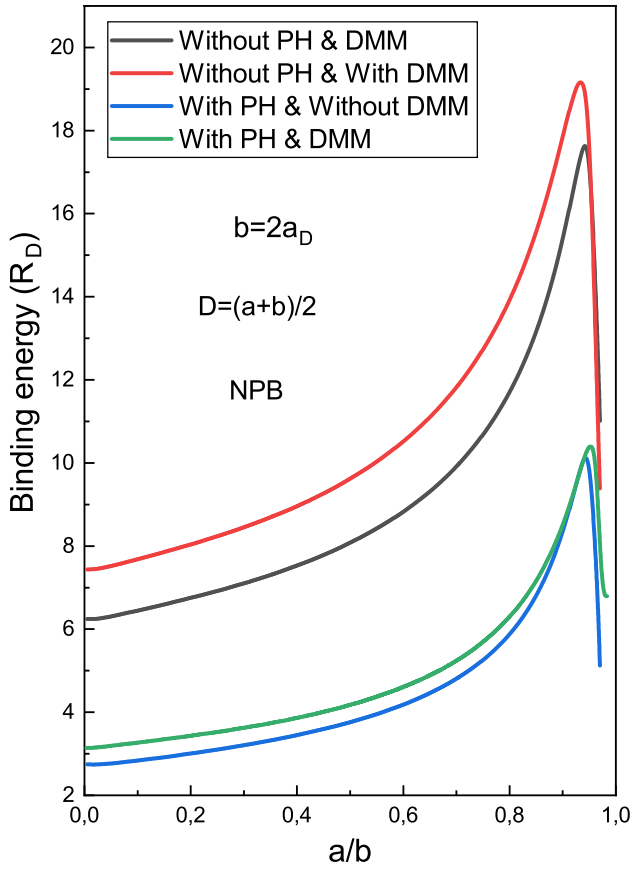


Fig. 10 Variation of the binding energy versus ratio a/b for $b = 2a_D$ in the band nonparabolicity case: Phonons and dielectric mismatch effects

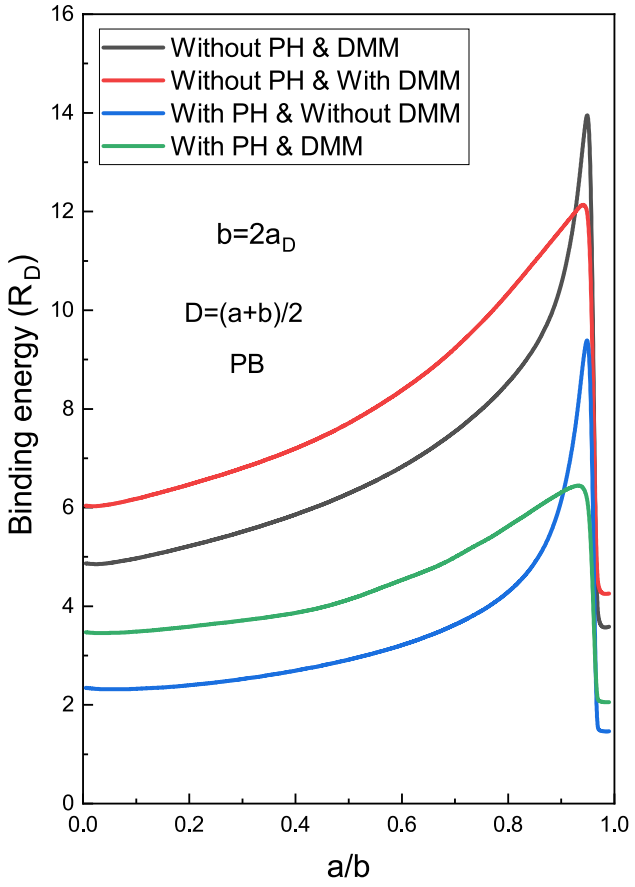


Fig. 11 The same as in Fig. 10 but for a parabolic conduction band description

to a variational description that leads to a given β-parameter. When doing so with phonons alone, the process leads to a different value of the parameter and, consequently, to a different outcome (which corresponds to another equilibrium state) and, therefore, to significant changes in the total and binding energies.

The nonparabolic description of the electron conduction band states leads to an increment of the binding energy for larger values of a/b, as seen from Figs. 10 and 11. This means that when both phonons and dielectric mismatch contributions are jointly taken into account, the conduction band nonparabolicity enhances the coupling between the carrier and the impurity in the strong confinement regime. This can be attributed to the NPB-induced increment in electron confinement and the consequent strengthening of electrostatic interaction. Let us now discuss the effect of dielectric mismatch. Assuming that interaction with LO-phonons is present, the results for E_b in this case appear plotted in Figs. 12 and 13, considering both the parabolic and nonparabolic descriptions for electron states in the conduction band of the structure. We have chosen to keep fixed the value of the dielectric constant inside the QD and to consider two different values of this quantity in the external dielectric medium. In all cases, one may observe that E_b augments as long as the ratio a/b increases due to the effective reduction of the electron-impurity distance associated with the narrowing of the potential confinement region. When $a = b$ the core/shell structure actually disappears and we are led to the simple case of an isolated spherical GaN QD in which the correction of the interaction with bulk-like LO phonons is explicitly considered. But if we focus on the dielectric mismatch effect it is possible to observe, clearly, that for the largest difference between the inner and outer values of the dielectric constant, there will be an increment of the electron-donor-impurity binding energy, when comparing with the uniform dielectric setup. One may attribute this phenomenon to the fact that the dielectric contrast acts as an additional negative -attractive- energy that enhances the electrostatic coupling between the electron and the Coulombic center, as can be noticed from Eqs. (17–20). This happens almost along with the entire range of a/b, with the exception of the range of values close to the unity in the parabolic model. There, the results for E_b without dielectric mismatch are higher. This indicates that, within the parabolic band approach, the

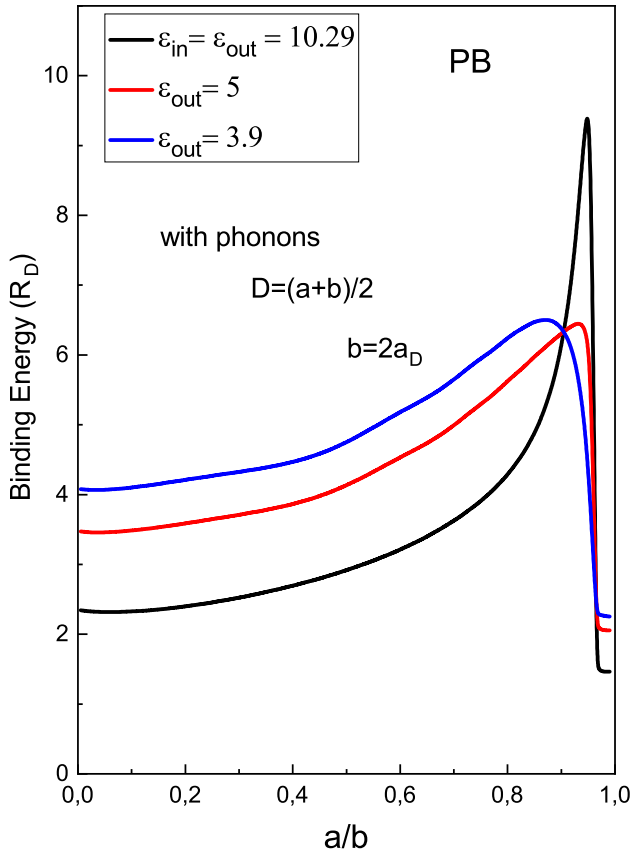


Fig. 12 Variation of the binding energy versus ratio a/b for $b = 2a_D$ for a parabolic band description and the inclusion of polaronic corrections; comparing the effects of absence or inclusion of dielectric mismatch effects

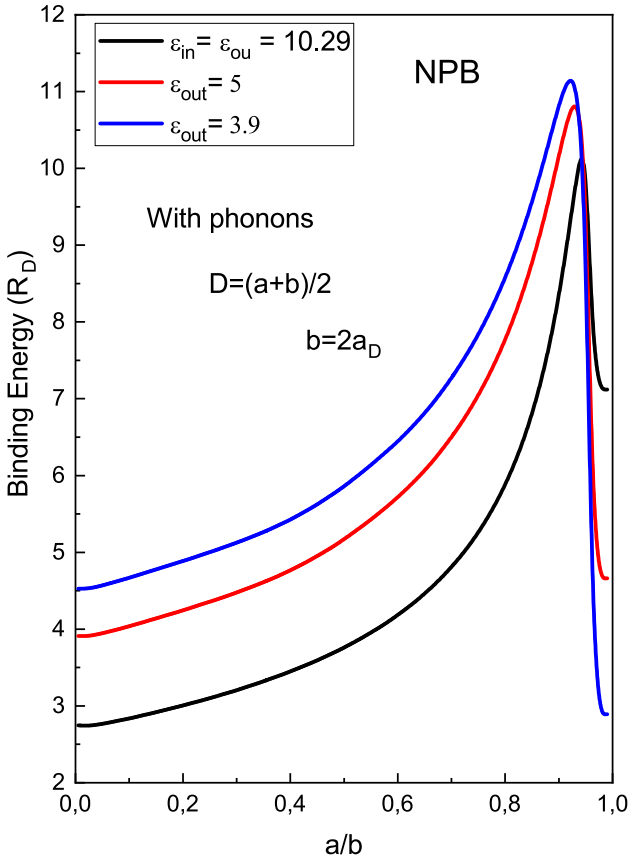


Fig. 13 The same as in Fig. 12 but for the nonparabolic conduction band model

competition between the geometric and dielectric confinements causes the weakening of the spatial localization of the electron wave function in the vicinity of the impurity atom. This picture has a change when the conduction band nonparabolicity is incorporated in the calculation. Again, the higher dielectric contrast implies a stronger electron-impurity coupling and bigger values of the binding energy, and E_b is quantitatively larger compared to the parabolic case and remains so along with the whole range of a/b. Clearly, the latter result is opposite to that resulting from the parabolic approach.

Looking for an explanation to the *NPB* effect one has to bear in mind that, in first place, the energy dependence of the electron effective mass implies an increment of this quantity in the *InN* shell. In consequence, both the polaron mass and the electron-phonon coupling constant have an increment as well. This implies that there is a stronger electron localization in the potential well region and also a stronger coupling with LO-phonons, but the first of these two effects tends to dominate and the result is the reduction of the effective electron-impurity distance which strengthens the electrostatic interaction and increases the binding energy. The significant reduction of E_b when a/b approaches unity and the dielectric contrast is larger relates with the opposite situation, which is explained by the corresponding behavior of the electron probability density (spatial distribution of the wave function). That is, the electron wave function has a greater part localized inside the *GaN* core region which makes the electron-impurity distance to augment (remember that when $a \simeq b$, the position of the impurity will be close to the outer *QD* interface). Also, taking into account the modification of the corresponding polaronic mass, the diminishing role played by the electron-phonon coupling becomes enhanced because its strength is larger in the *GaN*.

4 Conclusion

We have carried out a theoretical investigation on the properties of the donor-impurity-related electronic spectrum in a zincblende GaN/InN core/shell quantum dot with a spherical shape. Our study takes into account the effect of modifying the geometry of the structure by changing the internal and external radii and the position of the donor center. In

addition, the study includes the influence of the interaction between carrier and ionized impurity with longitudinal optical phonons in the structure, as well as the image charge phenomenon due to dielectric mismatch between the dot layers and the external medium in which it is embedded. In the description of the electron states, we have incorporated the influence of conduction band nonparabolicity through an energy-dependent modified carrier effective mass, which is affected by polaronic corrections.

We have found that, in general, both LO-phonon and dielectric mismatch have relatively important contributions to the impurity binding energy, with a quantitative reduction of its value that is less pronounced in the case of a nonparabolic band description. On the other hand, the higher the dielectric contrast between the quantum dot and its surrounding medium the larger will be the value of the binding energy in the system. Our results may contribute to the research work in this class of structures, revealing both the importance of the geometrical setup and the need of a more complete description in the form of including electron-phonon interaction and the problem of dielectric inhomogeneity.

Acknowledgements LMP and DL acknowledge partial financial support from FONDECYT 1180905. DL acknowledges partial financial support from Centers of excellence with BASAL/CONICYT financing, Grant AFB180001, CEDENNA. A. Tiutiunnyk acknowledges the financial support from Postdoctoral Fellowship FONDECYT 3180276. MEMR is thankful to Universidad de Medellín for support and hospitality during 2019-2020 sabbatical stay. He also acknowledges Mexican CONACYT for partial support through Grant A1-S-8218 (CB 2017-2018). AT and KN, acknowledge Moroccan Ministry of Higher Education and Research and CNRST (project: PPR/37/2015).

Compliance with ethical standards

Data availability statement The data that support the findings of this study are available from the corresponding author upon reasonable request.

Appendix A: Electrostatic potential created by a source charge placed in spherical nanostructure

This appendix gives the calculation main points of generalized Coulomb potential energy and self-polarization energy in spherical nanostructure/matrix. Those effects are coming from the surface charge densities emergence when two materials touch. The surface charge distributions depend, According to the image charge classical theory, on dielectric constants, sign of source charge and its distance to the interfaces. The very small size of low-dimensional structures reinforce the induced charge effect and make them significant. We note that this analytical calculation is based on calculations performed previously for different geometries [41, 68, 80–82].

Let us start by Poisson's equation describing the electrostatic potential created at $\vec{r} \equiv (r, \theta, \varphi)$:

$$\nabla^2 V\left(\vec{r}-\vec{s}\right) = -\frac{4\pi}{\varepsilon_{in}}\delta\left(\vec{r}-\vec{s}\right) \tag{A1}$$

In spherical coordinates, the right side of Eq. (A1) becomes:

$$\begin{aligned} -\frac{4\pi}{\varepsilon_{in}}\delta\left(\vec{r}-\vec{s}\right) = \\ -\frac{4\pi}{\varepsilon_{in}}\frac{1}{r^2}\delta(r-s)\delta\left(\cos(\theta)-\sin\left(\theta'\right)\right)\delta\left(\varphi-\varphi'\right) \\ = -\frac{4\pi}{\varepsilon_{in}}\frac{1}{r^2}\delta(r-s)\frac{1}{\sin(\theta)}\delta\left(\theta-\theta'\right)\delta\left(\varphi-\varphi'\right) \end{aligned} \tag{A2}$$

Using the spherical harmonics completeness relation, Eq. (A2) writes

$$\begin{aligned} -\frac{4\pi}{\varepsilon_{in}}\delta\left(\vec{r}-\vec{s}\right) \\ = -\frac{4\pi}{\varepsilon_{in}}\frac{1}{r^2}\delta(r-s)\sum_{l=0}^{+\infty}\sum_{m=-1}^{+1} Y_{l,m}(\theta,\varphi)Y_{l,m}\left(\theta',\varphi'\right) \end{aligned} \tag{A3}$$

Applying the addition theorem for spherical harmonics, Eq. (A3) can be written as:

$$-\frac{4\pi}{\varepsilon_{in}}\delta\left(\vec{r}-\vec{s}\right) = -\frac{1}{\varepsilon_{in}r^2}\delta(r-s)\sum_{l=0}^{+\infty}(2l+1)P_l(\cos(\xi)) \tag{A4}$$

where $P_l(\cos(\xi))$ is the Legendre polynomial of l order and ξ is the angle between $\vec{r} \equiv (r, \theta, \varphi)$ and $\vec{s} \equiv (s, \theta', \varphi')$. Supposing that the charge is sited on the z-axis, which means that $\theta' = 0$ and $\xi = \theta$, the Poisson equation expression becomes

$$\nabla^2 V\left(\vec{r}-s\right) = -\frac{1}{\varepsilon_{in}r^2}\delta(r-s)\sum_{l=0}^{+\infty}(2l+1)P_l(\cos(\theta)) \tag{A5}$$

Equation (A5), which is invariant with respect to the z-axis, can be solved by developing its solutions in the basis of Legendre polynomials:

$$V\left(\vec{r}-s\right) = \sum_{l=0}^{+\infty} V_l(r-s)P_l(\cos(\theta)) \tag{A6}$$

Expanding calculation using Eqs. (A5) and (A6), we get

$$\begin{cases} \frac{1}{r^2}\frac{d}{dr}\left(r^2\frac{dV_l(r,s)}{dr}\right) - \frac{l(l+1)}{r^2}V_l(r,s) = -\frac{1}{\varepsilon_{in}r^2}(2l+1), & r = s \\ \frac{1}{r^2}\frac{d}{dr}\left(r^2\frac{dV_l(r,s)}{dr}\right) - \frac{l(l+1)}{r^2}V_l(r,s) = 0, & r \neq s \end{cases} \tag{A7}$$

We search for solutions in the form $V_l(r,s) = C(s)r^m$. Proceeding with this we find that m may only take l

and $-(l+1)$ values. Thence, $V_l(r,s)$ can be given as $V_l(r,s) = C_1(s)r^l + C_2(s)r^{-(l+1)}$. The solutions of Eq. (A7) should respect these boundary conditions:

I. - $V_l^{QD}(r,s)$ must be regular for $r = 0$
II. - $V_l^{matrix}(r,s) \to 0$ when $r \to \infty$
III. - $V_l^{QD}(r,s)\Big|_{r=R^-} = V_l^{matrix}(r,s)\Big|_{r=R^+}$
IV. - $\varepsilon_{in} dV_l^{QD}(r,s)/dr\Big|_{r=R^-} = \varepsilon_{out} dV_l^{matrix}(r,s)/dr\Big|_{r=R^+}$
V. - Permutation of r and s must be verified i.e. $V_l^{QD}(r,s) = V_l^{QD}(s,r)$

Conditions I and II require that $r^{-(l+1)}$ and r^lcoefficients in nanostructure and in matrix, respectively, are equal zero. Thus, the solutions of Eq. (A7) in different regions write:

$$V_l(r,s) = \begin{cases} V_l^{QD}(r,s) = A(s)r^l, & r < s \\ V_l^{QD}(r,s) = B(s)r^l + \frac{C(s)}{r^{l+1}}, & s < r < R \\ V_l^{matrix}(r,s) = \frac{D(s)}{r^{l+1}}, & R < r \end{cases} \tag{A8}$$

The four unknown coefficients $A(s)$, $B(s)$, $C(s)$ and $D(s)$ are determined using the three conditions (3) to (5). The final Poisson equation solution, which contains Coulomb interaction between two charges placed at $\vec{r}$ and $\vec{s}$ as well as their interaction with surface charge densities at boundaries, writes:

$$V(r,s) = \begin{cases} V^{QD}(\vec{r},s) = \sum_{l=0}^{\infty} h\left(r^l s^l + \frac{1}{u}\frac{r^l}{s^{l+1}}\right) P_l(\cos(\theta)), & r < s \\ V^{QD}(\vec{r},s) = \sum_{l=0}^{\infty} h\left(s^l r^l + \frac{1}{u}\frac{s^l}{r^{l+1}}\right) P_l(\cos(\theta)), & s < r < R \\ V^{Matrix}(\vec{r},s) = \sum_{l=0}^{\infty} h\left(R^{2l+1} + \frac{1}{u}\right)\frac{s^l}{r^{l+1}} P_l(\cos(\theta)), & R < r \end{cases} \tag{A9}$$

To determine h, we integrate Eq. (A7) from $r-\kappa$ to $r+\kappa$, where κ is an infinitesimal value. Doing calculations, we find $h = u/\varepsilon_{in}$ where

$$u = (l+1)\left(\varepsilon_{in} - \varepsilon_{out}\right)/\left(l\varepsilon_{in} + (l+1)\varepsilon_{out}\right)R^{2l+1}. \tag{26}$$

Coulomb interaction between two particles:

The potential energy describing the interaction between a source charge q_1 and a target charge q_2 writes:

$$V_{q_1 \to q_2} = q_1 q_2 V(\vec{r},s) \tag{A10}$$

Doing calculations with $q_1 = e$; $q_2 = -e$,$r = r_e$, $s = D$ and $R = b$ it is not hard to find Eq. 8.

Self-polarization energy of single particle

The self-polarization energy $W_i(r_i)$ describing the interaction of a single-particle with surface charge distributions at material boundaries writes:

$$W_i(r) = \frac{1}{2}\left[V_{r>s}(\vec{r},s) + V_{s>r}(\vec{s},r)\right] \tag{A11}$$

Removing the terms $r_l/s_l + 1$ and $s_l/r_l + 1$ when $r < s$ and $s < r$ respectively which represent the pure Coulomb interaction term and by setting $q_1 = q_2 = e$ and $\theta = 0$ we can easily obtain Eq.7.

Appendix B: Polaron - induced screened Coulomb potential

This appendix briefly outlines the derivation of the polaron-induced modification of a Coulombic potential related with an ionized impurity center in a polar crystal. The formulation was originally put forward for excitons by Aldrich and Bajaj [84], following Haken results via Lee-Low-Pines (LLP) variational formalism [83]. Instead, the approach by Aldrich and Bajaj makes use of the free polaron variational wave function proposed by Haga [85]. The system consists of an electron coupled to the screened Coulomb potential, assumed to be located at the origin. The Hamiltonian writes:

$$H_0 = \frac{p^2}{2m} - \frac{e^2}{\varepsilon_\infty |\mathbf{r}|} + \sum_{\mathbf{q}} \hbar\omega b_q^+ b_q + \sum_{\mathbf{q}} \left[\gamma_q e^{i\mathbf{q}.\mathbf{r}} b_q + cc\right] \tag{B1}$$

where b_q^+ and b_q are the creation and annihilation LO phonon operators of wavevector $\mathbf{q}$, ω is the optical phonon frequency, p is the momentum of the electron and $\mathbf{r}$ its position coordinate. Besides, m is the conduction band mass.

The quantity γ_q is given as:

$$\gamma_q = -\frac{-i\hbar\omega}{q}\left(\frac{4\pi\alpha}{\beta V}\right)^{1/2}, \tag{B2}$$

where V is the crystal volume, $\alpha = 1/2\overline{\varepsilon}\left(e^2\beta/\hbar\omega\right)$ is the so-called Frölich constant, with $\beta = (2m\omega/\hbar)^{1/2}$. The quantity

$1/\bar{\varepsilon} = 1/\varepsilon_\infty - 1/\varepsilon_0$ is the inverse reduced dielectric constant, with ε_∞ and ε_0 being the static dielectric and high-frequency constants, respectively.

To derive the effective potential the model employs the following wavefunction:

$$\psi(\mathbf{r}) = \sum_{\mathbf{k}} C_k \phi_k\left(r, b_q^+\right) \tag{B3}$$

Where $\phi_k\left(r, b_q^+\right)$ is the free polaron wavefunction [85]:

$$\phi_k\left(r, b_q^+\right) = e^{i\mathbf{k}.\mathbf{r}} U\left(1 + \sum_q c_q b_q^+\right)|\phi_0\rangle \tag{B4}$$

where U is the LLP canonical transformation and $|\phi_0\rangle$ is the phonon vacuum state [86], and

$$c_q = 4i\left(\frac{\pi\alpha\beta^3}{V}\right)^{1/2} \frac{qe^{-i\mathbf{q}\cdot\mathbf{r}}}{(1+\alpha/2)(q^2+\beta^2)^2} \tag{B5}$$

The effective Hamiltonian for the poalron interacting with the screened Coulomb center arises from the expression $H = \langle\psi(\mathbf{r})|H_0|\psi(\mathbf{r})\rangle$:

$$H_{AB} = -\alpha\hbar\omega + \frac{p^2}{2m^*} + V_{AB}(r) \tag{B6}$$

where m^*, the Haga polaron mass, is defined as:

$$m^* = \frac{m(1+\alpha/6)}{1-\alpha/12} \tag{B9}$$

and

$$V_{AB}(r) = -\frac{e^2}{\varepsilon_\infty} + \frac{e^2\beta}{2\bar{\varepsilon}} \frac{e^{-\beta r}}{\left\{1+\alpha/\left[4(1+\alpha/12)^2\right]\right\}(1+\alpha/12)} + V_H(r) \tag{B9}$$

is the Aldrich-Bajaj modified electrostatic potential with

$$V_H(r) = \frac{e^2}{\bar{\varepsilon}r}\left(1 - \frac{e^{-\beta r}}{2}\right) \tag{B9}$$

representing the Haken-like potential. Thus, we are led to the Eq. (12) of the article.

References

1. P. Mélinon, S. Begin-Colin, J.L. Duvail, F. Gauffre, N.H. Boime, G. Ledoux, J. Plain, P. Reiss, F. Silly, B. Warot-Fonrose, Phys. Rep. **543**, 163 (2014)
2. A.R. Kortan, R. Hull, R.L. Opila, M.G. Bawendi, M.L. Steigerwald, P.J. Carroll, L. Brus, J. Am. Chem. Soc. **112**, 1327 (1990)
3. H.S. Zhou, I. Honma, H. Komiyama, J. Phys. Chem. **97**, 895 (1993)
4. A. Mews, A. Eychmuller, M. Giersig, D. Schooss, H. Weller, J. Phys. Chem. **98**, 934 (1994)
5. J.W. Haus, H.S. Zhou, I. Honma, H. Komiyana, Phys. Rev. B **47**, 1359 (1993)
6. H. Zhao, L. Jin, Y. Zhou, A. Bandar, Z. Fan, A.O. Govorov, Z. Mi, S. Sun, F. Rosei, A. Vomiero, Nanotechnology **27**, 495405 (2016)
7. W. Ji, P. Jing, W. Xu, X. Yuan, Y. Wang, J. Zhao, A.K.-Y. Jen, Appl. Phys. Lett. **103**, 053106 (2013)
8. T.-R. Kuo, S.-T. Hung, Y.-T. Lin, T.-L. Chou, M.-C. Kuo, Y.-P. Kuo, C.-C. Chen, Nanoscale Res. Lett. **12**, 537 (2017)
9. S. Kim, B. Fisher, H.-J. Eisler, M. Bawendi, J. Am. Chem. Soc. **125**, 11466 (2003)
10. J.J. Li, J.M. Tsay, X. Michalet, S. Weiss, Chem. Phys. **318**, 82 (2005)
11. R. Xie, U. Kolb, J. Li, T. Basché, A. Mews, J. Am. Chem. Soc. **127**, 7480 (2005)
12. V. Kamat Prashant, J. Phys. Chem. C **112**, 18737 (2008)
13. M. Bar, S. Lehmann, M. Rusu, A. Grimm, I. Kotschau, I. Lauermann, P. Pistor, S. Sokoll, T. Schedel-Niedrig, M.C. Lux-Steiner, C.-H. Fischerb, L. Weinhardt, C. Heske, Ch. Jung, Appl. Phys. Lett. **86**, 222107 (2005)
14. Z. Lu, Ch. Gao, Q. Zhang, M. Chi, J.Y. Howe, Y. Yin, Nano Lett. **11**, 3404 (2011)
15. L.C.L. Hollenberg, A.S. Dzurak, C. Wellard, A.R. Hamilton, D.J. Reilly, G.J. Milburn, R.G. Clark, Phys. Rev. B **69**, 113301 (2004)
16. X. Gao, Y. Cui, R.M. Levenson, L.W.K. Chung, S. Nie, Nat. Biotechnol. **22**, 969 (2004)
17. L. Igor, L. Medintz, A.R. Clapp, H. Mattoussi, E.R. Goldman, B. Fisher, J.M. Mauro, Nat. Mater. **2**, 630 (2003)
18. D. Vasudevan, R. Ranganathan, A. Trinchi, I. Cole, J. Alloy. Compd. **636**, 395 (2015)
19. J.Q. Grim, L. Manna, I. Moreels, Chem. Soc. Rev. **44**, 5897 (2015)
20. A.L. Rogach (ed.), *Semiconductor Nanocrystal Quantum Dots* (Springer, Wien, 2008)
21. B.O. Dabbousi, J. Rodriguez-Viejo, F.V. Mikulec, J.R. Heine, H. Mattoussi, R. Ober, K.F. Jensen, M.G. Bawendi, J. Phys. Chem. B **101**, 9463 (1997)
22. M.A. Hines, P. Guyot-Sionnest, J. Phys. Chem. **100**, 468 (1996)
23. M. Kria, M. El-Yadri, N. Aghoutane, L.M. Pérez, D. Laroze, E. Feddi, Chin. J. Phys. **66**, 444 (2020)
24. H. Bekhouche, A. Gueddim, N. Bouarissa, N. Messikine, Chin. J. Phys. **65**, 146 (2020)
25. R. Khordad, B. Vaseghi, Chin. J. Phys. **59**, 473 (2019)
26. M.G. Barseghyan, A. Manaselyan, A.A. Kirakosyan, L.M. Pérez, David Laroze. Phys. E **117**, 113807 (2020)
27. J. Jasieniak, M. Califano, S.E. Watkins, ACS Nano **5**, 5888 (2011)
28. O. Chen, Y. Yang, T. Wang, H. Wu, C. Niu, J. Yang, Y.C. Cao, J. Am. Chem. Soc. **133**, 17504 (2011)
29. A. Baranov, Y. Rakovich, J. Donegan, T. Perova, R. Moore, D. Talapin, A. Rogach, Y. Masumoto, I. Nabiev, Phys. Rev. B **68**, 1653061 (2003)
30. N. Gaponik, S.G. Hickey, D. Dorfs, A.L. Rogach, A. Eychmüller, Small **6**, 1364 (2010)
31. P.M. Koenraad, M.E. Flatté, Nat. Mater. **10**, 91 (2011)
32. M. Cristea, E.C. Niculescu, Eur. Phys. J. B **85**, 191 (2012)
33. M. Cristea, E.C. Niculescu, Phys. Lett. A **377**, 1221 (2013)
34. E.C. Niculescu, M. Cristea, J. Lumin. **135**, 120 (2013)
35. Z. Zeng, C.S. Garoufalis, A.F. Terzis, S. Baskoutas, J. Appl. Phys. **114**, 023510 (2013)
36. A.K. Manaselyan, A.A. Kirakosyan, Phys. E **22**, 825 (2004)
37. A.K. Manaselyan, M.M. Agasyan, A.A. Kirakosyan, Phys. E **14**, 366 (2002)
38. A. Talbi, E. Feddi, A. Oukerroum, E. Assaid, F. Dujardin, M. Addou, Superlatt. Microstruct. **85**, 581 (2015)
39. A. Talbi, E. Feddi, A. Zouitine, M. El Haouari, M. Zazoui, A. Oukerroum, F. Dujardin, E. Assaid, M. Addou, Phys. E **84**, 303 (2016)

40. A. Ibral, A. Zouitine, E. Assaid, E. Feddi, F. Dujardin, Phys. B **449**, 261 (2014)
41. A. Ibral, A. Zouitine, E. Assaid, H. El Achouby, E. Feddi, F. Dujardin, Phys. B **458**, 73 (2015)
42. A. Zouitine, A. Ibral, E. Assaid, F. Dujardin, E. Feddi, Superlatt. Microstruct. **109**, 123 (2017)
43. M. El-Yadri, N. Aghoutane, A. El Aouami, E. Feddi, F. Dujardin, C.A. Duque, Appl. Surf. Sci. **441**, 204 (2018)
44. S. M'zerd, M. El Haouari, A. Talbi, E. Feddi, M.E. Mora-Ramos, J. Alloy Compounds, **753**, 68 (2018)
45. M.A. Stroscio, M. Dutta, *Phonons in Nanostructures* (Cambridge University Press, Cambridge, 2003)
46. C. Trallero-Giner, R. Pérez-Alvarez, F. García-Moliner, *Long Wave Polar Modes in Semiconductor Heterostructures* (Elsevier, Oxford, 1998)
47. B.K. Ridley, *Electrons and Phonons in Semiconductor Multilayers*, 2nd edn. (Cambridge University Press, Cambridge, 2009)
48. M. El Haouari, M.E. Mora-Ramos, A. Talbi, E. Feddi, F. Dujardin, Phys. E **103**, 188 (2018)
49. P.G. Bolcatto, C.R. Proetto, Phys. Rev. B **59**, 12487 (1999)
50. V. I. Boichuk, I. V. Bilynsky, I. O. Shakleina and I. P. Kogoutiouk, J. Phys.:Conf. Ser. **289** (2011) 012004
51. A.L. Vartanian, A.L. Asatryan, L.A. Vardanyan, Superlatt. Microstruct. **103**, 205 (2017)
52. N. Sil, N. Daripa, A. Kapoor, S.K. Dey, Pramana-J. Phys. **90**, 7 (2018)
53. E.C. Niculescu, M. Cristea, U.P.B. Sci, Bull. Ser. A **75**, 195 (2013)
54. M. Cristea, A. Radu, E.C. Niculescu, J. Lumin. **143**, 592 (2013)
55. A.L. Vartanian, A.L. Asatryan, L.A. Vardanyan, Superlatt. Microstruct. **113**, 442 (2018)
56. S. Hong, J. Singh, J. Appl. Phys. **61**, 5346 (1987)
57. M. Cristea, E.C. Niculescu, Eur. Phys. J. B **85**, 191 (2012)
58. H. Frohlich, Proc. R. Soc. Edinburgh Sect. A: Math. **215**, 291 (1952)
59. C. Aldrich, K.K. Bajaj, Solid State Commun. **22**, 157 (1977)
60. K. K. Bajaj, in *Polarons in Ionic Crystals and Polar Semiconductors*, edited by J. Devreese, 194-225 (North-Holland, Amsterdam, 1972)
61. S. Shokhovets, O. Ambacher, G. Gobsch, Phys. Rev. B **76**, 125203 (2007)
62. Gh Safarpour, M.A. Izadi, M. Novzari, E. Niknam, M.M. Golshan, Commun. Theor. Phys. **61**, 765 (2014)
63. A. Radosavijevic, J. Radovanovic, V. Milanović, D. Indjin, Opt. Quant. Electron. **47**, 865 (2015)
64. P.G. Moses, C.G. Van de Walle, Appl. Phys. Lett. **96**, 021908 (2010)
65. I. Vurgaftman, J.R. Meyer, J. Appl. Phys. **94**, 3675 (2003)
66. M.K. Bose, K. Midya, C. Bose, J. Appl. Phys. **101**, 054315 (2007)
67. L.E. Brus, J. Chem. Phys. **80**, 4403 (1984)
68. J.M. Ferreyra, C.R. Proetto, Phys. Rev. B **57**, 9061 (1998)
69. C. Delerue, M. Lanoo (Eds.), *Nanostructures: Theory and Modeling* (Springer, Berlin, 2004)
70. C.J.F. Bättcher: *Theory of Electric Polarization, 2nd ed., V.1* (Elsevier, Amsterdam 1973)
71. E. Feddi, M. El Haouari, E. Assaid, B. Stèbè, J. El Khamkhami, F. Dujardin, Phys. Rev. B **68**, 235313 (2003)
72. T.D. Lee, F. Low, D. Pines, Phys. Rev. **90**, 297 (1953)
73. J. Pollmann, H. Büttner, Phys. Rev. B **16**, 4480 (1977)
74. A. A. Parvathi and A. John Peter, Acta Physica Polonica A **124** (2013) 706
75. Y.-F. Wu, X.-X. Liang, K.K. Bajaj, Chin. Phys. **14**, 2314 (2005)
76. P. Rinke, M. Winkelkemper, A. Qteish, D. Bimberg, J. Neugebauer, M. Scheffler, Phys. Rev. B **77**, 075202 (2008)
77. M. Feneberg, M. Röppischer, C. Cobet, N. Esser, J. Schörmann, T. Schupp, D.J. As, F. Hörich, J. Bläsing, A. Krost, R. Goldhahn, Phys. Rev. B **85**, 155207 (2012)
78. M.-Y. Xie, M. Schubert, J. Lu, P.O.Å. Persson, V. Stanishev, C.L. Hsiao, L.C. Chen, W.J. Schaff, V. Darakchieva, Phys. Rev. B **90**, 195306 (2014)
79. R. Cuscó, N. Doménech-Amador, S. Novikov, C.T. Foxom, L. Artús, Phys. Rev. B **92**, 075206 (2015)
80. L. Banyai, I. Galbraith, C. Ell, H. Haug, Phys. Rev. B **36**, 6099 (1987)
81. T. Takagahara, Phys. Rev. B **47**, 4569 (1993)
82. L.E. Brus, IEEE J. Quant. Electron. **22**, 1909 (1986)
83. H. Haken, Nuovo Cim. **10**, 1230 (1956)
84. C. Aldrich, K.K. Bajaj, Solid State Commun. **22**, 157 (1977)
85. E. Haga, Prog. Theor. Phys. Kyoto **13**, 555 (1955)
86. T.D. Lee, F. Low, D. Pines, Phys. Rev. **90**, 297 (1953)

Publisher's Note Springer Nature remains neutral with regard to jurisdictional claims in published maps and institutional affiliations.